Electronic Supplementary Material (ESI) for Catalysis Science & Technology.

Supporting Information

Operando diffuse reflectance UV-vis spectroelectrochemistry for investigating oxygen evolution electrocatalysts

Additional DRUV spectra

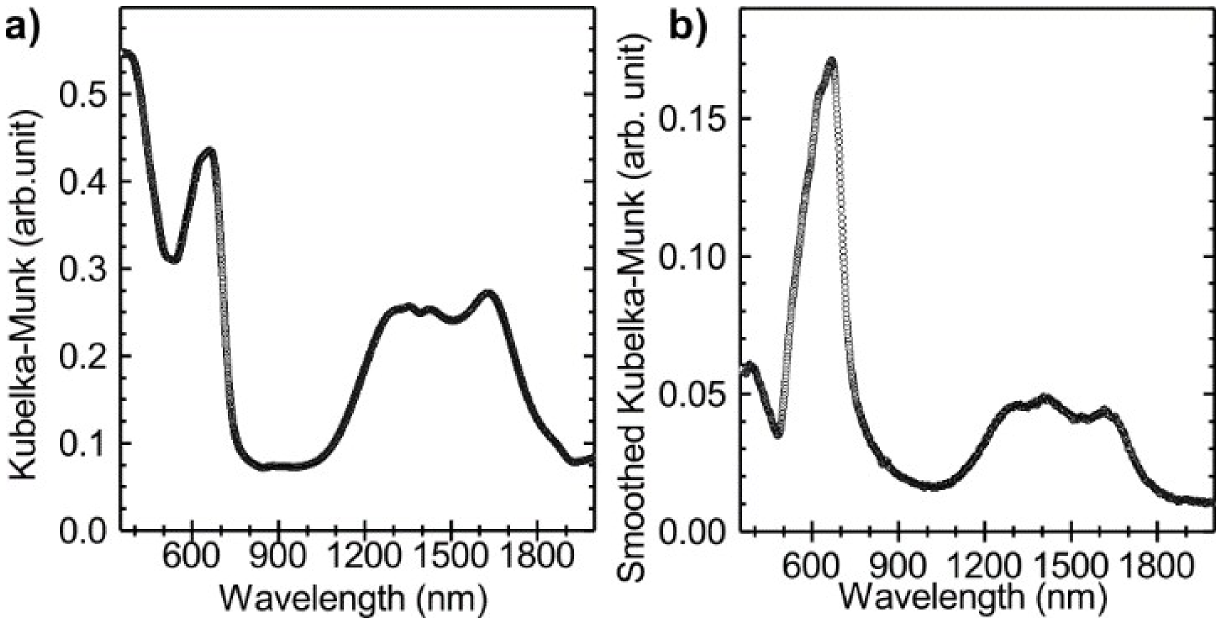

Figure S1. DRUV spectra of powdered $Zn_{0.35}Co_{0.65}O$ a) with $BaSO_4$ background and b) on Au working electrode of an SPE with the bare electrode as background.

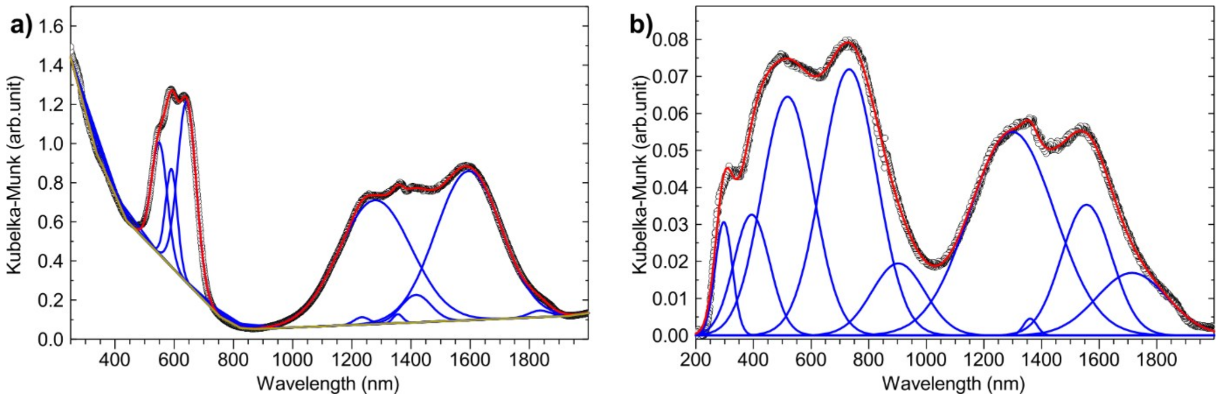

Figure S2. DRUV spectra of a) powdered $CoAl_2O_4$ nanoparticles and b) powdered CoO nanoparticles in rock salt structure as a reference for Co^{2+}_{oh}.

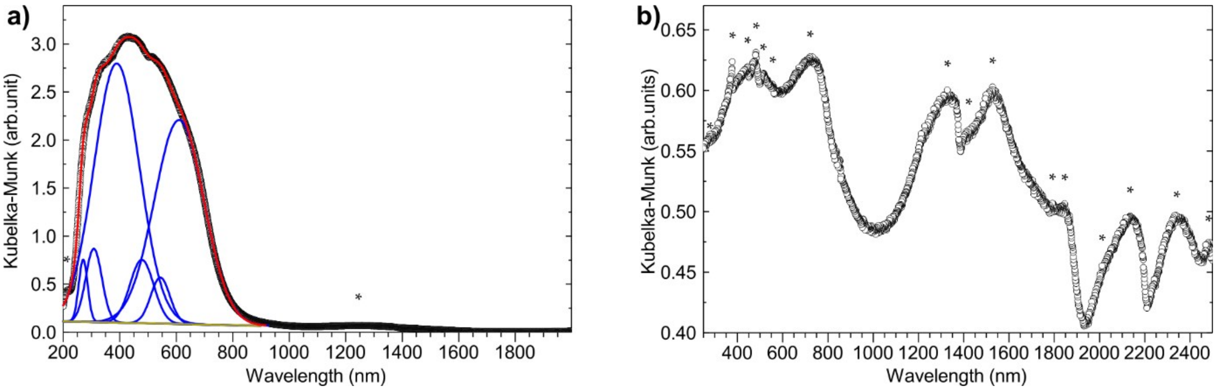

Figure S3. DRUV spectrum of a) powdered Co(O)OH nanoparticles and b) powdered $ZnCo_2O_4$ nanoparticles as references for Co^{3+}_{oh}. Asterisks mark peak positions not fitted.

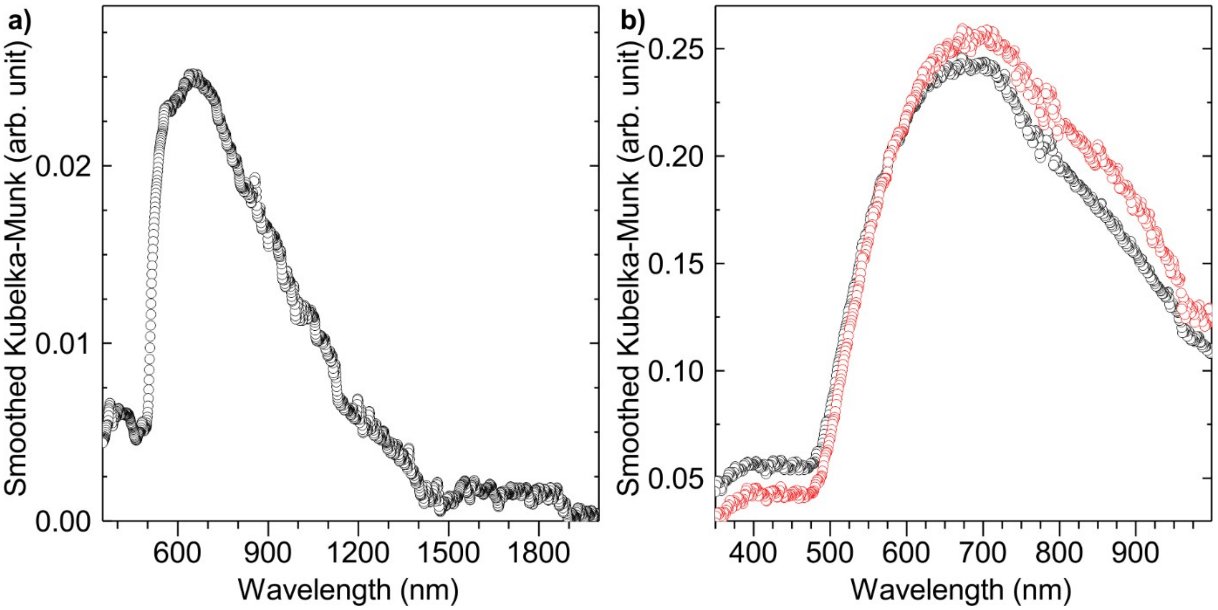

Figure S4. a) *Operando* DRUV spectrum of $Zn_{0.35}Co_{0.65}O$ at 1.3 V vs RHE showing also the NIR range. b) *Operando* DRUV spectra of $Zn_{0.35}Co_{0.65}O$ at 1.3 V vs RHE at oxidation (black) and reduction (red).

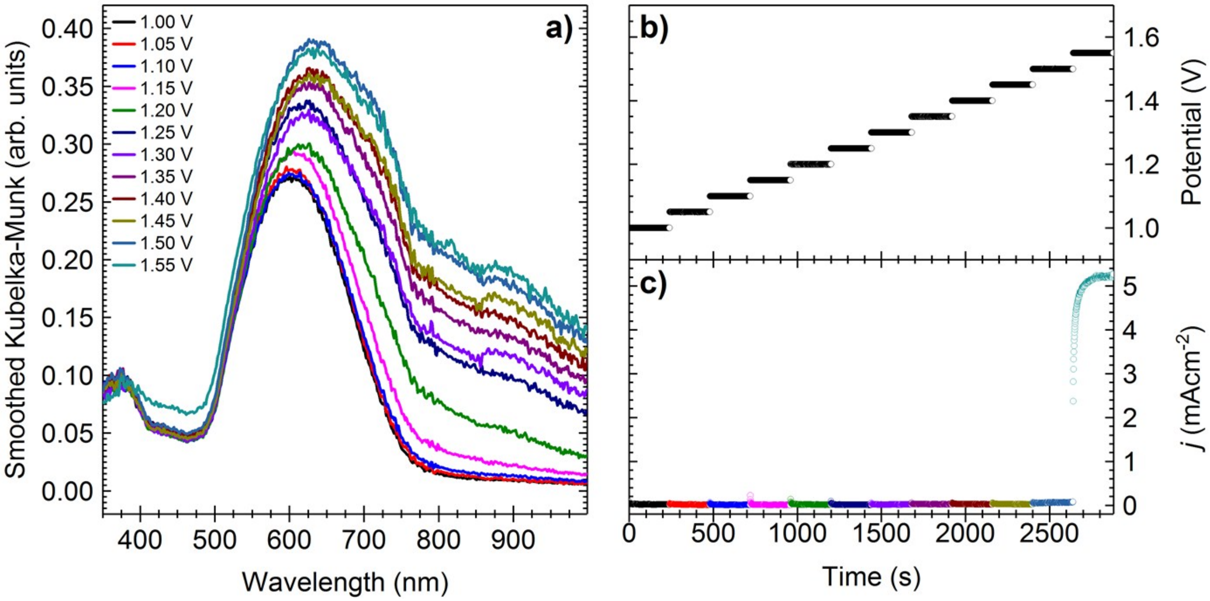

Figure S5. *Operando* DRUV spectroelectrochemistry of Co(O)OH nanoparticles. a) DRUV spectra of Co(O)OH in 1 M KOH, b) potential as a variation of time, c) CA measurements show the current density as a function of time. The colors correspond to the potential.

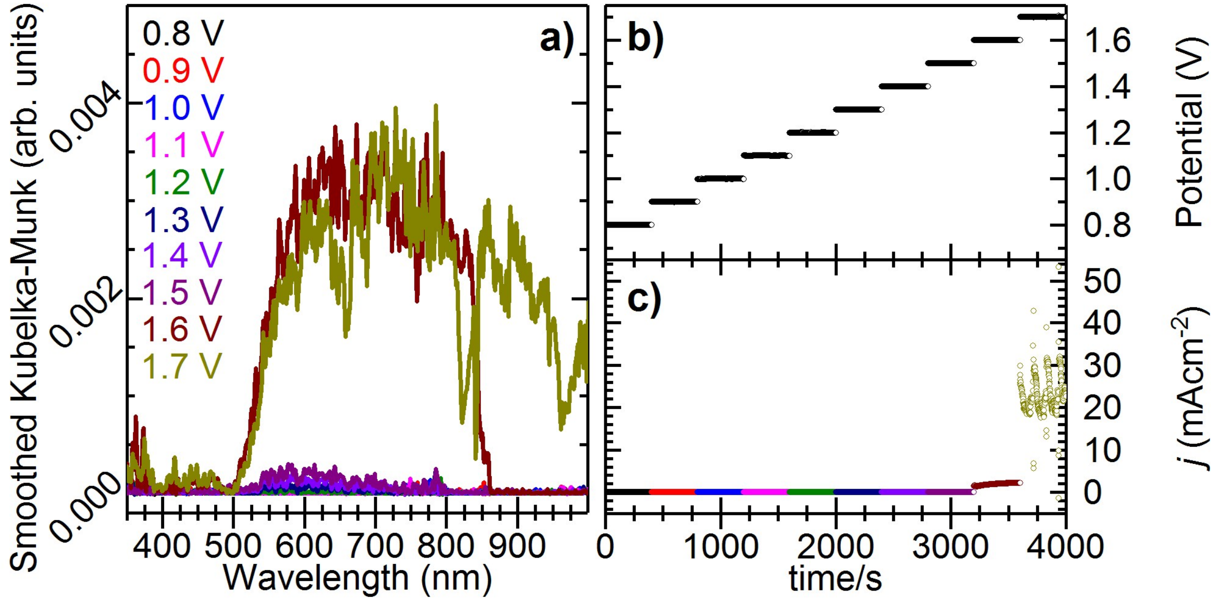

Figure S6. *Operando* DRUV spectroelectrochemistry of the SPE without loading as the control. a) DRUV spectra of SPE 250AT in 1 M KOH, b) potential as a variation of time, c) CA measurements show the current density as a function of time. The colors correspond to the potential.

Calculating the amount of Co oxidized during the operando measurement

The integration of the current in a CA measurement gives access to the charge transferred during the chosen time interval. Assuming all current is Faradaic, integrating the current for the time the spectra changed in **Fig. 1c** and **h**, i.e. between 1.0 V and 1.2 V, a charge of 1.25 mC is obtained. By division by the Faraday constant (96485 C/mol), the amount of transferred electrons is 0.0130 µmol. This charge can now be correlated to the initial sample loading, which was 10 µg (2 µL of catalyst ink (5 mg/mL) on the SPE). The estimated molar mass of $Zn_{0.35}Co_{0.65}O$ is 77.19 g/mol, and thus the loading on the SPE was 0.130 µmol of catalyst or 0.084 µmol of Co. Thus, 15.4 % of all initially contained Co^{2+} atoms are oxidized during this time.

When integrating the oxidation peak of the $Co^{2+/3+}$ redox couple in the first CV cycle of $Zn_{0.35}Co_{0.65}O$ (**Fig. 5a** in Reference 20, scan rate: 20 mV/s), a charge of 0.45 mC is obtained. The initial loading of catalyst was 3 µg (3 µL catalyst ink (1 mg/mL) on glassy carbon), which equals 0.039 µmol catalyst or 0.025 µmol Co. Correlating the charge to the initial loading, 18.5 % of all contained Co^{2+} atoms are oxidized in the first CV cycle. This is in good agreement of the value obtained from the *operando* measurement. However, this analysis does not take into account cobalt species dissolved during the measurement.

Integration of the current at 1.4 V, where the oxidation $Co^{3+/4+}$ is expected and the contribution of the OER should be still very small, yields a charge of 0.62 µC. Calculating the ratio between Co^{4+}/Co^{3+}, a value of 49.8 % is obtained. Thus, half of the contained Co^{3+} is oxidized to Co^{4+}.

DRUV band assignments

In the following tables, bands were assigned to transitions predicted by the according Tanabe-Sugano diagrams taken from R.J. Lancashire.[1] Bands written in parentheses were assigned to the nearest transition based on the approximated values for B and Δ/B, but need to be treated with caution. In the last column, the expected positions of the assigned bands are given, based on the according Tanabe-Sugano diagram. The band positions are obtained manually by selecting the maximum intensity of a band or the position of a shoulder or by Gaussian peak deconvolution.

Table S1. Band positions and assignment for DRUV spectrum of powdered $CoAl_2O_4$ nanoparticles in **Figure S1a**. The bands are assigned assuming tetrahedral Co^{2+} (d^7). Transitions are derived from Tanabe-Sugano diagram for d^3 octahedral (approximated values: B = 806 cm^{-1}, Δ/B = 4.9).

Wavelength	**Wavenumber**	**assigned transition**	**expected at**
[/nm]	[/cm^{-1}]		[/nm]
1854 1585 1405 1257	5394 6309 7117 7955	fine structure of $^4A_2(F) \rightarrow {}^4T_1(F)$	1458
1362	7342	2v(OH) harmonic band	
634	15 773	$^4A_2(F) \rightarrow {}^2E(G)$	631
577	17 007	$^4A_2(F) \rightarrow {}^4T_1(P)$	585
549	18 215	$^4A_2(F) \rightarrow {}^2A_1(G)$	553
< 500	> 20000	unassigned transitions	

Table S2. Band positions and assignment for DRUV spectrum of powdered CoO nanoparticles in **Figure S1b**. The bands are assigned assuming octahedral Co^{2+} (d^7) in a weak field. Transitions are derived from Tanabe-Sugano diagram for d^7 octahedral (approximated values: B = 933 cm^{-1}, Δ/B = 7.9).

Wavelength	**Wavenumber**	**assigned transition**	**expected at**
[/nm]	[/cm^{-1}]		[/nm]
1714 1556 1297	5835 6425 7708	fine structure of $^4T_{1g}(F) \rightarrow {}^4T_{2g}(F)$	1582
1360	7351	2v(OH) harmonic band	
903	11078	not assigned	
732	13658	$^4T_{1g}(F) \rightarrow {}^4A_{2g}(F)$	732
518	19301	$^4T_{1g}(F) \rightarrow {}^4T_{1g}(P)$	518
394	25394	$({}^4T_{1g}(F) \rightarrow {}^2T_{2g}(H))$	387
297	33682	$({}^4T_{1g}(F) \rightarrow {}^2E_g(D))$	305

Table S3. Band positions and assignment for DRUV spectrum of powdered Co(O)OH nanoparticles in **Figure S2a**. The bands are assigned assuming octahedral Co^{3+} (d^6) in a strong field. Transitions are derived from Tanabe-Sugano diagram for d^6 octahedral (approximated values: B = 777 cm^{-1}, $\Delta/B = 23.7$).

Wavelength	Wavenumber	assigned transition	expected at
[/nm]	[/cm^{-1}]		[/nm]
1244	8039	${}^1A_{1g}(I) \rightarrow {}^3T_{1g}(H)$	1118
610	16393	${}^1A_{1g}(I) \rightarrow {}^1T_{1g}(I)$	610
544	18382	(splitting of ${}^1T_{1g}(I)$ state)	
478	20921		
389	25707	${}^1A_{1g}(I) \rightarrow {}^1T_{2g}(I)$	389
308	32468	$({}^1A_{1g}(I) \rightarrow {}^3T_{2g}(G))$	311
271	36900	(splitting of free-ion ${}^1G$ state)	
213	46948	$({}^1A_{1g}(I) \rightarrow {}^3T_{1g}(G))$	212

Table S4. Band positions and assignment for DRUV spectrum of powdered $ZnCo_2O_4$ nanoparticles in **Figure S2b**. The bands are assigned assuming octahedral Co^{3+} (d^6) in a strong field. Transitions are derived from Tanabe-Sugano diagram for d^6 octahedral (approximated values: B = 661 cm^{-1}, $\Delta/B = 23.6$).

Wavelength	Wavenumber	assigned transition	expected at
[/nm]	[/cm^{-1}]		[/nm]
2482	4029	Unassigned	
2341	4272		
2136	4682		
2011	4973		
1845	5420	(fine structure of ${}^1A_{1g}(I) \rightarrow {}^5T_{2g}(D)$)	1567
1791	5583		
1527	6549		
1422	7032		
1327	7536	${}^1A_{1g}(I) \rightarrow {}^3T_{1g}(H)$	1327
721	13870	${}^1A_{1g}(I) \rightarrow {}^1T_{1g}(I)$	721
555	18018	fine structure of ${}^1A_{1g}(I) \rightarrow {}^1T_{2g}(I)$ and higher transitions	459
514	19455		
483	20747		
444	22523		
377	26525		
281	35587		

Table S5. Band positions and assignment for DRUV spectrum of powdered $Zn_{0.35}Co_{0.65}O$ nanoparticles with $BaSO_4$ background in **Figure 2a**. The bands are assigned assuming tetrahedral Co^{2+} (d^7). Transitions are derived from Tanabe-Sugano diagram for d^3 octahedral (approximated values: B = 776 cm^{-1}, Δ/B = 4.6).

Wavelength	Wavenumber	assigned transition	expected at
[/nm]	[/cm^{-1}]		[/nm]
1867	5356	fine structure of ${}^4A_2(F) \rightarrow {}^4T_1(F)$	1596
1629	6139		
1426	7013		
1325	7547		
1355	7380	2v(OH) harmonic band	1567
661	15129	${}^4A_2(F) \rightarrow {}^2E(G)$	657
622	16077	${}^4A_2(F) \rightarrow {}^4T_1(P)$	618
575	17391	${}^4A_2(F) \rightarrow {}^2A_1(G)$	582
377	26525	$({}^4A_2(F) \rightarrow {}^2E(D))$	372

Table S6. Band positions and assignment for DRUV spectrum of $Zn_{0.35}Co_{0.65}O$ on SPE in **Figure 2b**. The bands are assigned assuming tetrahedral Co^{2+} (d^7). Transitions are derived from Tanabe-Sugano diagram for d^3 octahedral (approximated values: B = 768 cm^{-1}, $\Delta/B = 4.7$).

Wavelength [/nm]	**Wavenumber** [/cm^{-1}]	**assigned transition**	**expected at** [/nm]
1615 1535 1409 1310	6192 6515 7097 7634	fine structure of $^4A_2(F) \rightarrow {}^4T_1(F)$	1580
667	14993	$^4A_2(F) \rightarrow {}^2E(G)$	664
624	16026	$^4A_2(F) \rightarrow {}^4T_1(P)$	621
580	17241	$^4A_2(F) \rightarrow {}^2A_1(G)$	586
382	26178	$(^4A_2(F) \rightarrow {}^2E(D))$	373

Table S7. Band positions and assignment for DRUV spectrum of $Zn_{0.35}Co_{0.65}O$ on SPE in 1 M KOH in **Figure 4a**. The bands are assigned assuming octahedral Co^{2+} (d^7). Transitions are derived from Tanabe-Sugano diagram for d^7 octahedral (approximated values: B = 827 cm^{-1}, $\Delta/B = 10.2$).

Wavelength [/nm]	**Wavenumber** [/cm^{-1}]	**assigned transition**	**expected at** [/nm]
632	15823	$(^4T_{1g}(F) \rightarrow {}^4A_{2g}(F)$ and/or splitting of ^2G free ion term)	633
533	19762	$^4T_{1g}(F) \rightarrow {}^4T_{1g}(P)$	534
396	25253	$(^4T_{1g}(F) \rightarrow {}^2T_{1g}(H))$	395

Table S8. Band positions and assignment for DRUV spectrum of $Zn_{0.35}Co_{0.65}O$ on SPE at 0.9 V vs RHE in 1 M KOH in **Figure 4b**. The bands are assigned assuming octahedral Co^{2+} (d^7). Transitions are derived from Tanabe-Sugano diagram for d^7 octahedral (approximated values: B = 791 cm^{-1}, $\Delta/B = 10.7$).

Wavelength [/nm]	**Wavenumber** [/cm^{-1}]	**assigned transition**	**expected at** [/nm]
630	15873	$(^4T_{1g}(F) \rightarrow {}^4A_{2g}(F)$ and/or splitting of ^2G free ion term)	630
548	18248	$^4T_{1g}(F) \rightarrow {}^4T_{1g}(P)$	548
407	24570	$(^4T_{1g}(F) \rightarrow {}^2T_{1g}(H))$	407

Additional information on $CoAl_2O_4$

Figure S5 shows the Al2p, C1s and O1s XPS spectra. In **Figure S5a**, the main peak is that of the Al2p, the two other peaks at higher binding energies correspond to the Au $4f_{7/2}$ and $4f_{5/2}$ (at 84.0 eV and at 87.7 eV, respectively) and the rising intensity at lower binding energy is due to Co3p. In Fig. S5b), the C1s peaks in **Figure S5b** are shifted by 5.1 eV (before reaction) and 3.8 eV (after reaction) as compared to the expected energy for adventitious carbon (~284.8 eV) [2]. The O1s spectra in **Figure 5c** also shows high binding energy peaks, which match well the energy shifts observed for the C1s. In addition, we observed that the core level of all the elements, except for those of gold, were subject to rigid energy shifts to lower binding when reducing the X-ray intensity (not shown here) indicating that charging of the $CoAl_2O_4$ film occurs upon irradiation. Given that XPS is a surface sensitive technique, this further shows that part of the analyzed area includes uncovered gold patches. Consistently, to correct for the sample charging, rigid shifts of 5.1 eV and 3.8 eV were applied to the spectra before and after reaction, respectively. Note that this procedure was also applied to the Co spectra shown in the main text. With this, we obtain consistent binding energies for all the elements. After reaction, we remark minor rigid shifts of the Co2p, Al2p and O1s core level as mentioned in the main text, which are attributed to changes in the Fermi level.

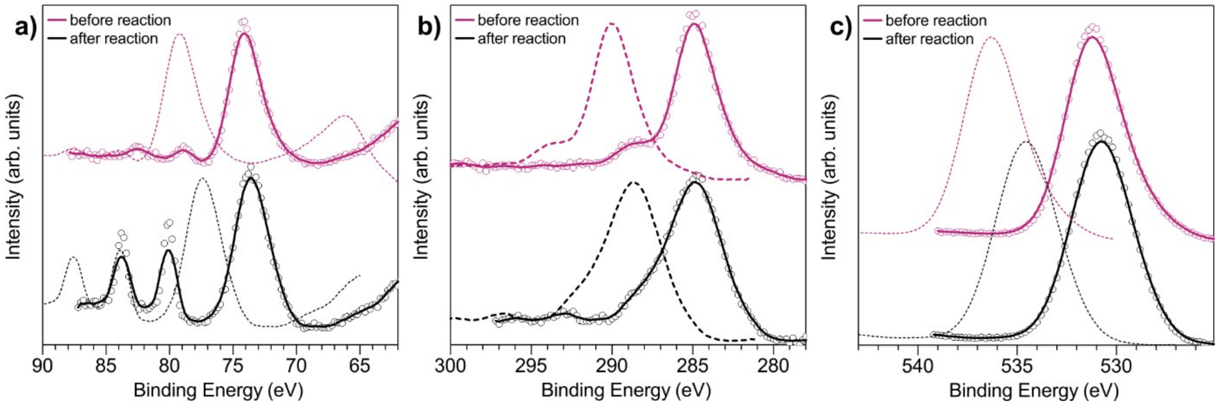

Figure S7. XPS spectra on a) the Al edge, b) the C edge and c) the O edge before and after 1 h electrochemical reaction at 10 mAcm^{-2}. Dashed lines represent the measured spectra, solid lines the corrected.

Table S9. EXAFS fit parameters at the Co-K edge for $CoAl_2O_4$ after electrochemical reaction. The amplitude reduction factor was fitted first from the Co-foil to reduce the number of variables.

				Path	*N*	*R*(Å)	σ²(Å²)	Δ*E* (eV)	±*R*(Å)	±σ²(Å²)	±Δ*E* (eV)
***R*-factor**	0.0235	N_{idp}	17.6	Co-O1	4	1.999	0.0053	2.831	0.012	0.0009	1.622
S_0^2	0.83195	N_{var}	11	Co-Al1	12	3.295	0.0135	-7.468	0.020	0.0015	2.020
***R*-range fit**	1.15 – 3.6	χ^2	863	Co-O2	12	3.331	0.0135	2.831	0.020	0.0015	1.622
***k*-range fit**	3.2 – 11.0	$\chi^2_{red.}$	132	Co-Co1	4	3.444	0.0135	-7.468	0.020	0.0015	2.020

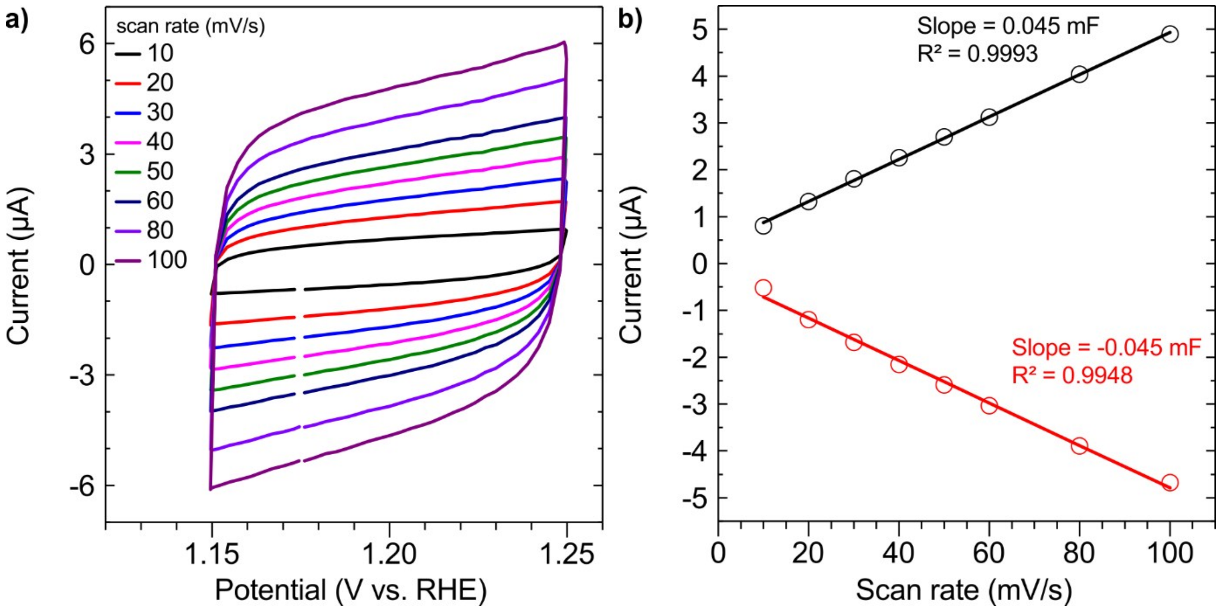

Figure S8. a) Double-layer capacitance (C_{dl}) measurements of $CoAl_2O_4$ for determining the electrochemically active surface area (*ECSA*) in 1 M KOH. 3rd cycle out of 5 cyclic voltammograms that were measured with different scan rates in the non-Faradaic region (100 mV potential window around 1.2 V vs RHE). b) The anodic (black) and cathodic (red) charging currents versus the scan rate. The data-points are the currents measured at 1.2 V, averaged over the last 4 CV cycles of each scan rate. The double-layer capacitance is calculated as the average of the absolute slopes of the linear fit. The values calculated are: C_{dl} = 0.045 mF, *ECSA* = 1.13 cm² and roughness R_f = 15.99.

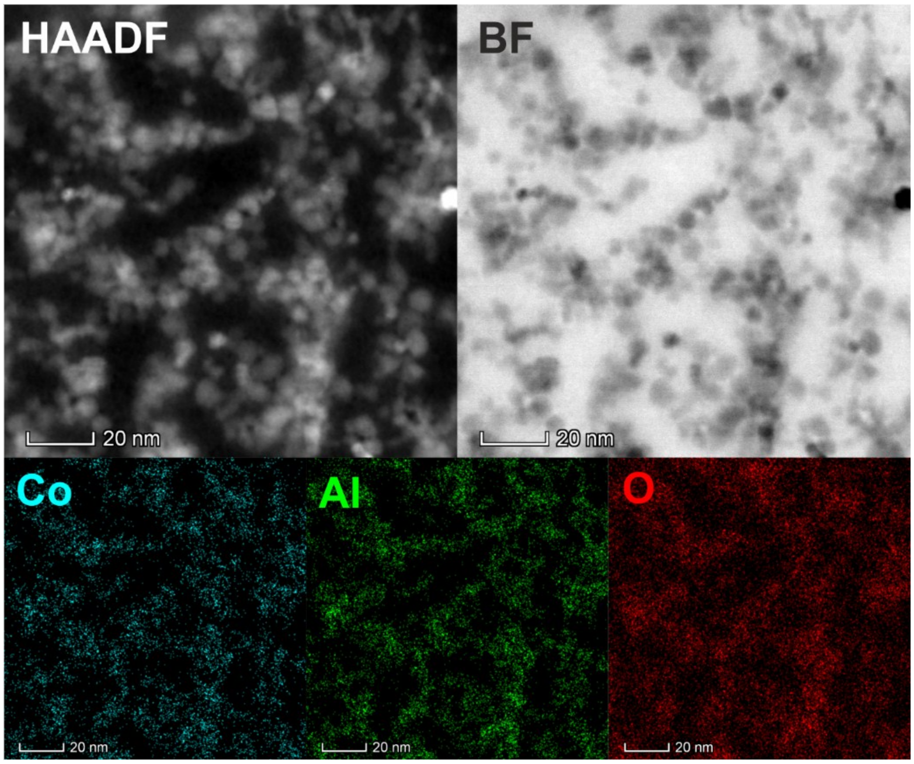

Figure S9. STEM HAADF and bright field micrographs and EDX mapping of cobalt, aluminum, and oxygen in $CoAl_2O_4$ before the reaction.

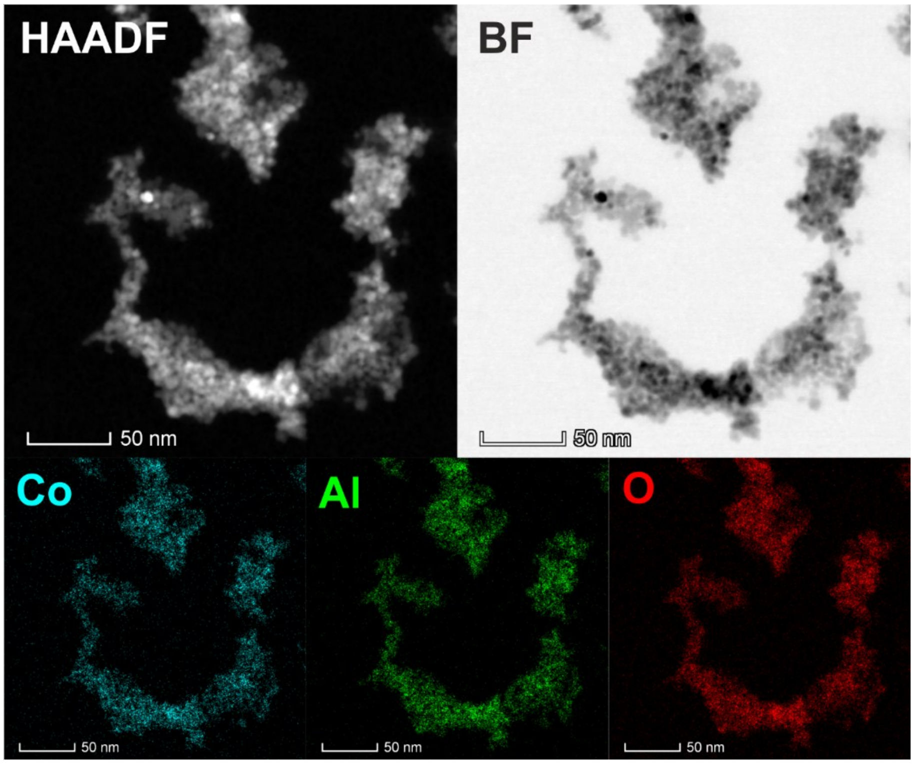

Figure S10. STEM HAADF and bright field micrographs and EDX mapping of cobalt, aluminum, and oxygen in $CoAl_2O_4$ after the reaction.

Calculation of aluminum atoms in top most nanoparticle shell

Following Lippens' and Lannoos equations 3a and 3b, the number N of atoms in a particle is related to the numbers of shells.[3] If we approximate a spherical shape for our particles, and take into account only the diameter of the largest (smallest) particles, which is 7.4 nm (4.6 nm), we can approximate a volume for one nanoparticle V_{NP} = 212,175 Å^3 (V_{NP} = 50,965 Å^3). Since the crystal structure is known, also the lattice parameter is known (a = 8.10670). From this the volume of a unit cell is V_{UC} = 532.76 Å^3. Furthermore, in a spinel, the unit cell is constructed of oxygen atoms in a face-centered cubic cell, i.e. in closed cubic packing. Thus, a unit cell contains 32 O, and 16 Al and 8 Co atoms in the octahedral and tetrahedral voids, respectively. Thus, the total number of O atoms can be derived from **Equation S1** to be n_O = 12744 (n_O = 3061). This corresponds, according to Lippens and Lannoo, to a particle consisting of 25 to 26 shells (15 to 16 shells). For 26 shells, 1564 atoms would be located in the top most shell (564 for 16 shells). Thus, ~11 % (~18 %) of all atoms are located in the top most shell.

$$n_O = 32 * \frac{V_{NP}}{V_{UC}} \tag{S1}$$

The EDX results in **Table 1** indicate an Al content of 60 %, which means a 10 % decrease compared to the perfect unit cell, where the Al content is 66.67 %. Thus, we can approximate, that all leached aluminum can origin from the top most layer.

Electrochemical properties of studied materials in comparison to other cobalt systems

Table S10. Comparison of electrochemical properties of different cobalt oxide based catalysts. Modified version of Table 1 on page 6 in Wahl et al.[4] Reproduced and modified with permission from WILEY-VCH. Copyright 2019 WILEY-VCH.

Catalyst	*ECSA* [cm²]	R_f[a)]	η[b)] [mV]	Tafel slope[c)] [mVdec^{-1}]
$Zn_{0.35}Co_{0.65}O$	21.93	310.18	322	42.6
$CoAl_2O_4$	1.13	15.99	362	44.8
Co_3O_4	0.91	12.81	365	48.1
$ZnCo_2O_4$	1.07	15.12	369	51.5
Co(O)OH	5.71	80.77	382	--
CoO	1.68	23.71	369	--

[a)] Roughness: *ECSA* divided by geometric area (7.069 mm^{-2}); [b)] at 10mA cm^{-2} in 1 M KOH; [c)] measured in 0.1 M KOH under quasi-stationary conditions

Operando cells

The main design considerations for the SEC were based on minimizing the optical path to maximize the yield of reflected light. A large electrolyte reservoir was avoided by using a peristaltic pump flushing the cell with the electrolyte. By this, the evolving gases as well as dissolved species origin from the catalyst surface are carried away from the electrode. Thus, all measured activity can be assigned to the heterogeneous catalyst, and activity arising from homogeneous catalysts can be excluded. Despite of the low cell profile, a reversible hydrogen electrode (RHE) is used as the reference electrode. A schematic overview of the SEC can be found in Fig. S11 (see Experimental for detailed description and Fig. S12 for photographs).
As a proof of concept Fig. S1 shows two spectra taken with the same spectrophotometer configuration: $Zn_{0.35}Co_{0.65}O$ in powder form with a $BaSO_4$ background (a) and applied on the gold working electrode of an SPE with the bare electrode as background (b). The comparison shows an overall decreased intensity when measuring on the SPE, and a decrease in absorptions arising from Zn at lower and Co transitions at higher wavelengths. Although, the transitions of Co are clearly visible and show no energetic shift, and thus, an SPE with an Au WE is suitable to measure structural properties of cobalt containing samples.

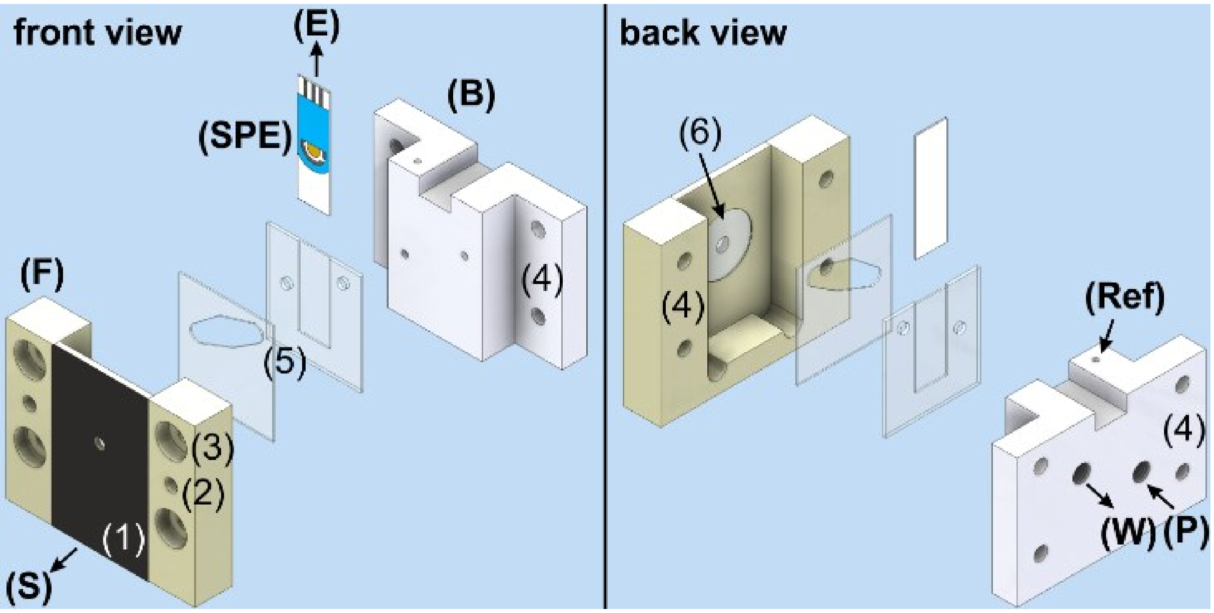

Figure S11. Design of the *operando* DRUV SEC. The PEEK front part (**F**) is covered with a black foil (1) and attached to the spectrophotometers (**S**) reflectance port by a mount and hold in place by magnets glued in cavities (2). The front is connected to the PTFE back (**B**) by nuts fixed in (3) and wing bolts going through holes (4). The electrode (**SPE**) is placed in the silicone gaskets (5) and connected to the potentiostat (**E**) by a connector cable. A Quartz window (6) is glued by silicone in a shallow cavity. The tip of the RHE reference electrode (**Ref**) is in contact to the electrolyte in the inlet channel. The electrolyte is flushed by a peristaltic pump (**P**) through PTFE tubes connected with HPLC fittings to the reservoir and the waste (**W**). A 3D-printed cover protects the setup from ambient light.

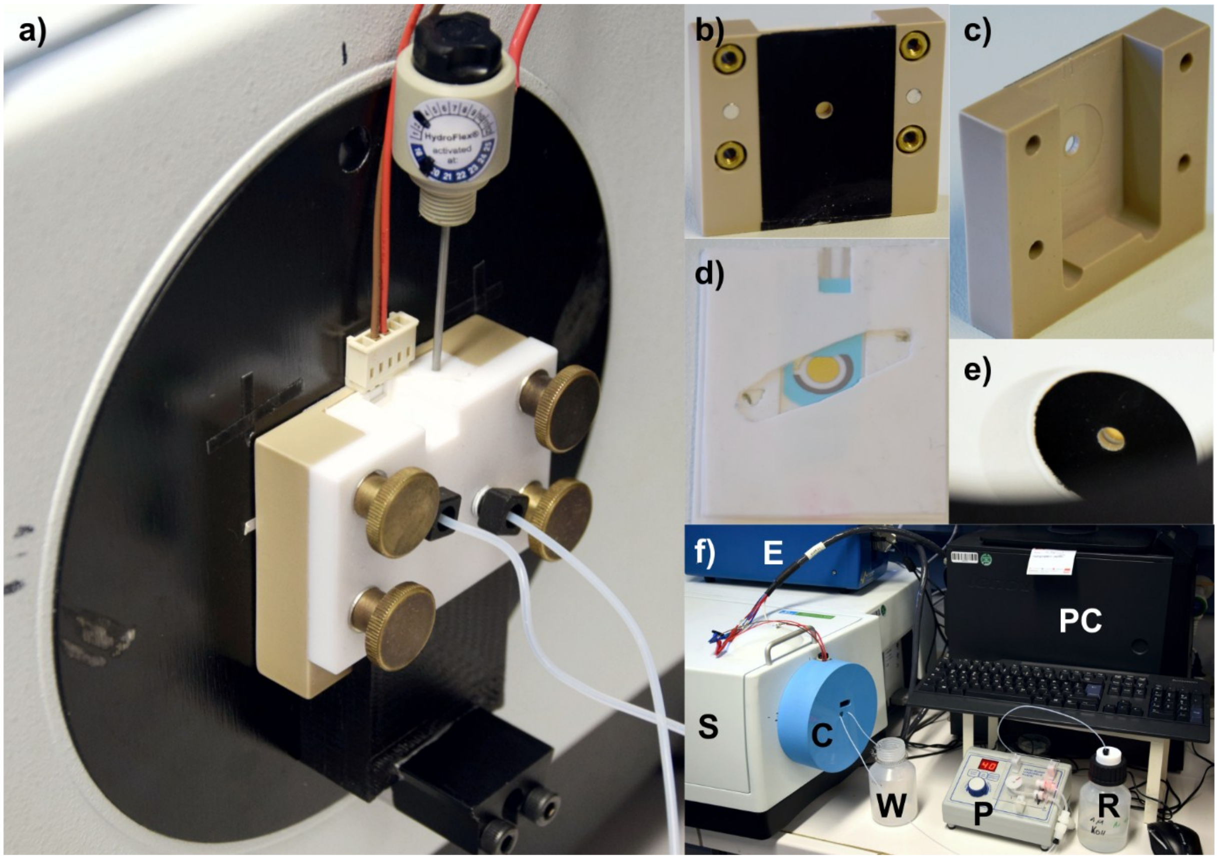

Figure S12. Photographs of the *operando* DRUV cell. a) Cell mounted at the reflectance port of the UV-vis spectrophotometer, equipped with the RHE. b) Front view of the PEEK part, covered with black absorbing foil. c) Back view of the PEEK part. d) Silicone gaskets and flow channel, equipped with the SPE. e) View in the integrating sphere showing the front of the cell and the Au working electrode. f) Full view of the setup. **S** is the UV-vis spectrophotometer, **E** is the potentiostat, **C** the 3D-printed cover. Through the cover go the electronic connections to the potentiostat and the tubes connecting the cell to the waste **W** and the peristaltic pump **P** that supplies the cell with electrolyte from the reservoir **R**. The spectrophotometer and the potentiostat are connected to the processing unit (**PC**).

Predecessor model of the cell.

The predecessor model of the *operando* cell used a plastic cuvette window instead of a Quartz window, limiting its wavelength range to the UV-visible. Instead of using silicone gaskets, a PTFE gasket was glued with silicone to the front part of the cell, to direct the flow of the electrolyte. The intention to redesign the cell was based on optimizing the flow of electrolyte as well as on making it more transferable to other kind of measurements, like *operando* X-ray absorption spectroscopy.

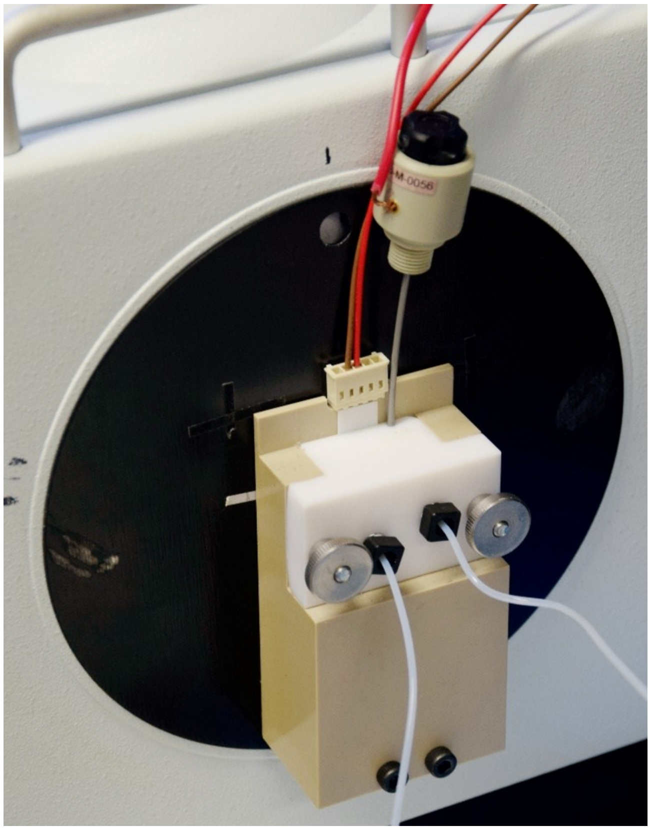

Figure S13. Photograph of the predecessor *operando* cell mounted on the reflectance port of the UV-vis spectrophotometer, equipped with the RHE and connected to the potentiostat, the pump and the waste.

References

1. R. J. Lancashire, Tanabe-Sugano diagrams via spreadsheets, http://wwwchem.uwimona.edu.jm/courses/Tanabe-Sugano/TSspread.html, (accessed May 13, 2019, 2019).
2. M. Jacquemin, M. J. Genet, E. M. Gaigneaux and D. P. Debecker, *ChemPhysChem*, 2013, **14**, 3618-3626.
3. P. E. Lippens and M. Lannoo, *Physical review. B, Condensed matter*, 1989, **39**, 10935-10942.
4. S. Wahl, S. M. El-Refaei, A. G. Buzanich, P. Amsalem, K.-S. Lee, N. Koch, M.-L. Doublet and N. Pinna, *Adv. Energy Mater.*, 2019, **9**, 1900328.